

Experimental investigation of the performance of a liquid fuel-fired porous burner operating on kerosene-vegetable cooking oil (VCO) blends for micro-cogeneration of thermoelectric power



K.F. Mustafa ^{a,*}, S. Abdullah ^a, M.Z. Abdullah ^b, K. Sopian ^a, A.K. Ismail ^c

^a Department of Mechanical and Materials Engineering, Faculty of Engineering and Built Environment, Universiti Kebangsaan Malaysia, UKM Bangi, Selangor 43600, Malaysia

^b School of Mechanical Engineering, Universiti Sains Malaysia Engineering Campus, Seri Ampangan, 14300 Nibong Tebal, Penang, Malaysia

^c Mechanical Section, Universiti Kuala Lumpur Malaysian Spanish Institute, Kulim Hi-Tech Park, Kedah 09000, Malaysia

ARTICLE INFO

Article history:

Received 21 April 2014

Accepted 21 August 2014

Available online 16 September 2014

Keywords:

Porous burner

Kerosene

Vegetable cooking oil

Thermoelectric

Emission

ABSTRACT

Studies related to porous burner for thermoelectric (TE) power generation have mainly focused toward achieving a specific range of power output for various applications. However, detailed analyses on the performance and emission aspects of the porous burner are lacking. In addition, physical integration between the burner and TE modules has added further complexity in this research area. Thus, this work aims to comprehend the effects of fuel–air equivalence ratio on the performance and emission characteristics of a liquid fuel-fired porous burner for micro-cogeneration of TE power. A catalytically inert Al_2O_3 porous medium was incorporated into a liquid fuel-fired porous burner operating on four mixtures of kerosene-vegetable cooking oil (VCO) blends: 100 kerosene, 90/10 KVCO, 75/25 KVCO, and 50/50 KVCO. Ten bismuth-telluride TE cells were arranged in a ten-sided polygon that, together with finned dissipators, formed a TE module electrically connected in series but thermally connected in parallel. The performance aspects at various fuel–air equivalence ratios were thoroughly evaluated with the corresponding temperature profiles, voltage, current, power output, and electrical efficiency. Results indicated that the surface temperature of the porous media was generally higher than the developed and exit flame temperature of the burner. Varying the fuel–air equivalence ratio significantly affected the electrical efficiency, with a maximum and minimum value of 1.94% and 1.10%, respectively. The power output steadily increased in the lean region, but stabilized as the fuel–air equivalence ratio slowly increased beyond the stoichiometric ratio. The CO emission was relatively lower at the lean region; however, significant amount was recorded in the rich combustion region. Moreover, NO_x fluctuated between 1 ppm and 4 ppm over the entire range of fuel–air equivalence ratio.

© 2014 Elsevier Ltd. All rights reserved.

1. Introduction

The present method of supplying the insatiable global energy demand has become clearly unsustainable. In addition, fossil fuel reserves, once hardly ever given a second thought, are now evidently exhaustible. The imminent dwindling of world's oil production and the numerous concerns related to future energy security are gradually showing that our key reliance on fossil fuel combustion is on the verge of reaching its critical peak. Furthermore, the ever-changing variability in our climatic ecosystems has obvious repercussions towards the overall intrinsic web of energy

production and utilization. The combination of these factors has prompted considerable efforts in the quest for feasible renewable energy sources to mitigate various environmental and socio-economic impacts caused by fossil-based fuels combustion. The search for renewable energy sources should provide a harmonious balance between sustainable development and environmental conservation.

Vegetable oils are renewable source of energy and fall under one of the subcategories of liquid biofuels, others being (i) bioalcohols and (ii) biocrude and synthetic oils [1,2]. Vegetable oils are abundantly available from diverse resources. They are non-polluting, locally available, easily accessible [3], and the triglycerides in their chemical structure contain considerable amount of oxygen [4]. Vegetable oils are generally derived from plants, and their combustion leads to recyclable carbon dioxide with greener

* Corresponding author. Fax: +60 4 5941025.

E-mail address: mekhairil@usm.my (K.F. Mustafa).

environment because of their negligible sulfur content [5]. As alternative engine fuels, vegetable oil blends have been successfully demonstrated as an effective substitute in diesel engine [6–10]. However, high viscosity and low volatility have been identified as major offenders to long-term engine operation. Comprehensive performance tests using vegetable oils have been evaluated in a cooking stove [11] operating on vegetable oils and kerosene blends [12], as well as in a pressure stove [13], vaporizing burner [14], and industrial boiler [15]. The exhaustive results obtained from these studies indicated that vegetable oils can be adopted as an alternative renewable fuel without major hardware modifications to the system components.

Vegetable oils and kerosene are liquid fuels. Liquid fuels are comparatively difficult to vaporize, require substantial combustion times [40], and exhibit propensity to coke [36]. Some liquid fuels also have poor volatility and tend to aggravate clogging at the fuel injector or fuel supply line. Using pressurized or preheated air to assist fuel atomization and vaporization is beneficial; however, concomitant reduction in the conversion efficiency commonly occurs. Driven by the desire to attain cleaner combustion of liquid fuels, porous media combustion provides an alternative option and viable solution compared with normal combustion. Porous media combustion involves significant enhancement of the conduction and radiation mode of heat transfer compared with conventional free flame combustion. The concept is appealing, and unsurprisingly, multitudes of ongoing research efforts on the applicability of porous media in liquid fuel combustion have been reported [37–39,41,45–48]. The combustion characteristics of a kerosene-fueled burner with multiple porous media configurations were explored [37] and subsequently broadened to stretch the extension limit of fuel–air equivalence [38]. The issues pertinent to high viscosity of biofuels was successfully demonstrated by Bakry et al. [39], who elucidated porous media combustion in vegetable oil-fueled burner. Vegetable oil is a prominent candidate as renewable energy source because its combustion can suppress the emission levels compared with conventional fuels.

Interest in thermoelectric (TE) power generation has also attracted a great deal of attention as an alternative means of power generation, as manifested by the recent upsurge of research activities related to TE generators [16–29]. Salient features of a TE device, such as its compactness, noiseless, robustness, remarkable reliability without physical moving parts [19,28,30], and minimal maintenance [49], have made this power generation pathway a noticeable research direction over other conventional power generators. The combustion-driven TE power device converts the temperature gradient between a hot source and a cold sink into electricity by capturing the photons of electron movement in the semiconductor materials of TE cells. The hot source is commonly a burner, which is practically powered by gaseous or liquid hydrocarbon fuels. Various gaseous fuels with excellent availability, such as natural gas [16,30], propane [18], hydrogen [19], dimethyl ether [31], and butane [26,32,33] have been investigated, covering wide array of variables, to elucidate the performance of TE power generation systems. Meanwhile, studies on liquid fuel-fired burner for TE power generation are limited, and development has been modest and remains largely unexplored. The literature is categorically limited to JP8 aviation fuel [34] and methanol [35]. Liquid fuels are easier to handle, relatively safer to transport, and possess greater energy density compared with conventional lithium-ion batteries [36]. Despite these apparent advantages, specific challenges associated to liquid fuels have hampered their prevalent use as primary fuel in TE systems. Reported studies [37–39,41] have primarily focused on burner performance, and integration to TE modules has not been discussed. Nevertheless, the idea of utilizing kerosene or kerosene-vegetable oil blend burner with TE system in

the foreseeable future seems to be an interesting proposition, which is environmentally sustainable and can result in a concomitant increase in the overall conversion efficiency of the TE power generation system.

Thus far, although encouraging results have been generally reported in liquid fuel combustion, the common disadvantage lies in the requirement of high pressure injector for fuel atomization or preheated air to aid fuel vaporization. Given that an external pumping device consumes electricity, this technique lessens the optimum operating range of the porous burner, thereby reducing the overall efficiency of the system [45]. Conversely, non-spray method is much more practical because the capillary action of the porous material negates the need of fuel pumping action, and can thus offset the potential pitfalls in system efficiency. The method is practically beneficial as discussed in Refs. [41,45–48]; however, these studies represent only few of the meaningful studies that examined non-spray porous burners. Reintroducing the concept in a porous burner for TE power generation brings additional flexibility in terms of component placement and space requirement because the fuel feeding system is merely gravitational. After the necessity of high pressure injector is eliminated, the focus shifts on regulating the temperature of the hot source for TE device, which can be achieved by active means, such as a cold and hot fluid circuit [24], or passive means, such as varying the fuel–air equivalence ratio of the porous burner. Manipulating the fuel–air equivalence ratio of the porous burner circumvents the need for additional devices, and the thermal input conditions can be varied accordingly. This method of adjusting the fuel–air equivalence ratio distinguishes itself from other common approach by several advantages, such as (i) optimum input temperature to TE cells, (ii) extended lean flammability limit, (iii) wider operational range for the porous burner and TE power output, and (iv) reduced emission level. Given that the proposed design in this work entails the incorporation of TE cells at the exit of the porous burner, the input temperature to the TE cells occurs as the flame develops near the exit of the porous burner. The temperature profiles at the surface of the porous media and the developed flame temperatures in the porous burner will be greatly affected by the variation of input variables; thus, these temperatures have to be measured and analyzed.

This study attempts to elicit the effect of the various combustion characteristics of liquid fuel-fired porous burner for TE power generation. The primary input variables including the fuel–air equivalence ratio and the corresponding temperature and emission (CO and NO_x), as well as the output power of the TE modules are thoroughly explained. This study aims to characterize the liquid fuel-fired porous burner and the corresponding TE voltage, current, and power output under a range of fuel–air equivalence ratio. Comparisons are presented for a porous burner operating on both pure kerosene and kerosene-vegetable cooking oil (VCO) blends.

2. Materials and methods

2.1. Fuel preparation and properties

Kerosene was purchased from a local store (sold in 1 kg bottle) and VCO was bought from a local supermarket (prepacked in 5 kg bottle). Prior to the tests, three blends of kerosene and VCO (mass basis) were prepared. These blends were 90/10 KVCO (90% by mass of kerosene with 10% by mass of VCO), 75/25 KVCO (75% kerosene and 25% VCO), and 50/50 KVCO (50% kerosene and 50% VCO). These fuels were blended in an ultrasonic homogenizer (UH FS-1200, Life Scientz, China) with a probe diameter of 13 mm. The process involved intense agitation of the fuel blends because of the transmission of high frequency electrical energy into the piezoelectric

Table 1

Measured properties and their corresponding instrument used for all tested fuels.

Property	Instrument	100 kerosene	90/10 KVCO	75/25 KVCO	50/50 KVCO
Density, kg/m ³	Pycnometer (Blaubrand, Germany)	794	800	819	844
Dynamic viscosity at 40 °C, Ns/m ²	Viscometer (LVDV-11+P, Brookfield, USA)	0.00164	0.00382	0.0115	0.0182
Surface tension, N/m	Surface tensiometer (Fisher Scientific, USA)	0.03300	0.03430	0.03250	0.03580
Flash point, °C	Flash point tester (PMA4 Pensky-Martens, Germany)	67	71	82	94
Lower heating value, MJ/kg	Adiabatic bomb calorimeter (Nenken 1013B, Japan)	45.42	44.91	42.14	42.90

transducer. Each fuel mixture took approximately 65 min to form a complete and uniform blending. The fuel samples were kept in a transparent container and observed for up to three weeks for any physical separation to ensure that the fuel properties remained consistent throughout the blend. The fuels were completely miscible, and no separation was visually observed. Three samples of blended fuels (90/10 KVCO, 75/25 KVCO, and 50/50 KVCO), with 100 kerosene (100% by mass of kerosene), were analyzed to determine the thermophysical properties using various instrument listed in Table 1.

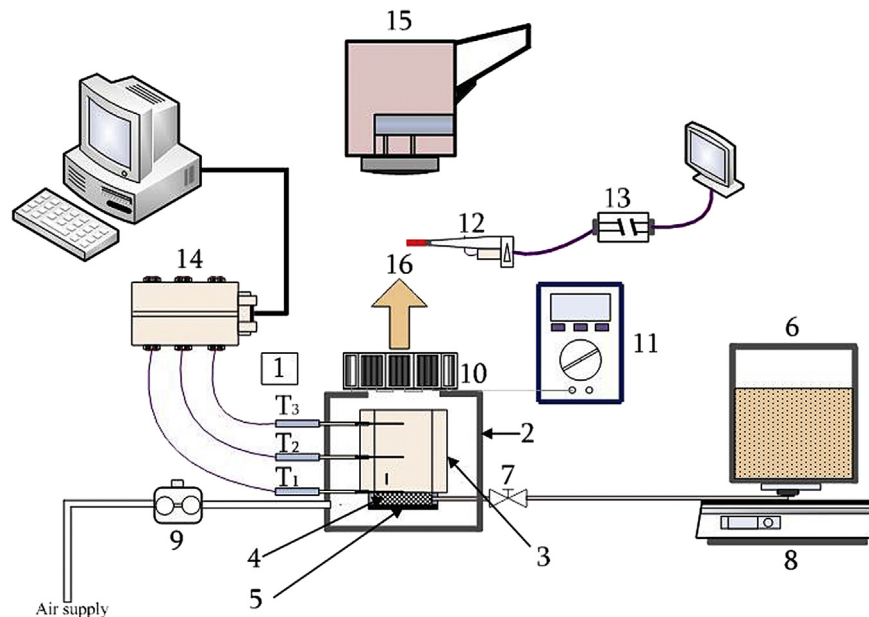
2.2. Experimental setup

The schematic of the experimental set-up is illustrated in Fig. 1. The experimental set-up employed in the laboratory essentially consists of the following components: (1) K-type thermocouples, (2) cylindrical combustion chamber, (3) flame holder, (4) porous alumina, (5) porous alumina housing, (6) fuel container, (7) fuel control valve, (8) electronic mass balance, (9) air flow meter, (10) TE module and cooling fin dissipators, (11) digital multimeter, (12) sampling probe, (13) cooled and dried sensors, (14) data acquisition system, (15) FLUKE Ti27 thermal imager, and (16) exhaust flow. A photograph of the experimental set-up is shown in Fig. 2. The position of porous alumina in the cylindrical combustion chamber is depicted in Fig. 3.

Fig. 4 shows the layout and dimensions of the chamber. The cylindrical combustion chamber was made of stainless steel with a thickness of 0.5 mm, a diameter of 250 mm and a height of 300 mm. The flame holder is a cylindrical chamber made of mild steel with a thickness of 0.5 mm. The flame holder, which consists of two

concentric cylinders: the inner circular cylinder with a diameter of 104 mm and the outer cylinder with a diameter of 142 mm, was used to stabilize the flame during the burner operation [13]. Perforated holes with a diameter of 3 mm each were created, surrounding the entire surface of the inner circular cylinder. A swirling air inlet was created by drilling a tangential slot at the periphery of the primary cylindrical combustion chamber at a horizontal position of 95 mm from the datum line. The air for combustion was supplied from a laboratory compressed air source, and was filtered and dried prior to the entrance of the primary combustion chamber. Flexible polyurethane tubes with an internal diameter of 6 mm were used to connect the air supply from the laboratory source to the experimental apparatus. The porous alumina housing had a bowl shape, with a diameter of 90 mm and a height of 12 mm. The porous alumina housing also has a 1.5 mm diameter hole that allows fuels to flow when the fuel valve was adjusted. The porous alumina (Al₂O₃) (Goodfellow Cambridge Limited, UK) used in this study was a foam type with a thickness of 12.7 mm and porosity of 86% and 8 pores/cm. The thermal conductivity of the alumina is 35 W/mK. The porous alumina was cemented to ensure proper fitting with the housing.

A glass fuel container was placed beside the primary cylindrical combustion chamber and used for all types of fuel blends tested in this study. The fuel supply line that connects the glass fuel container to the porous alumina housing had an inclination of 3° to the horizontal datum line. The elevated position of the fuel container ensured continuous and appropriate monitoring of the fuel supply to the porous media when the fuel valve was adjusted [11]. The fuel flow rate to the porous alumina through the fuel supply line was manually adjusted by a fine control valve.

**Fig. 1.** Schematic of the experimental set-up.

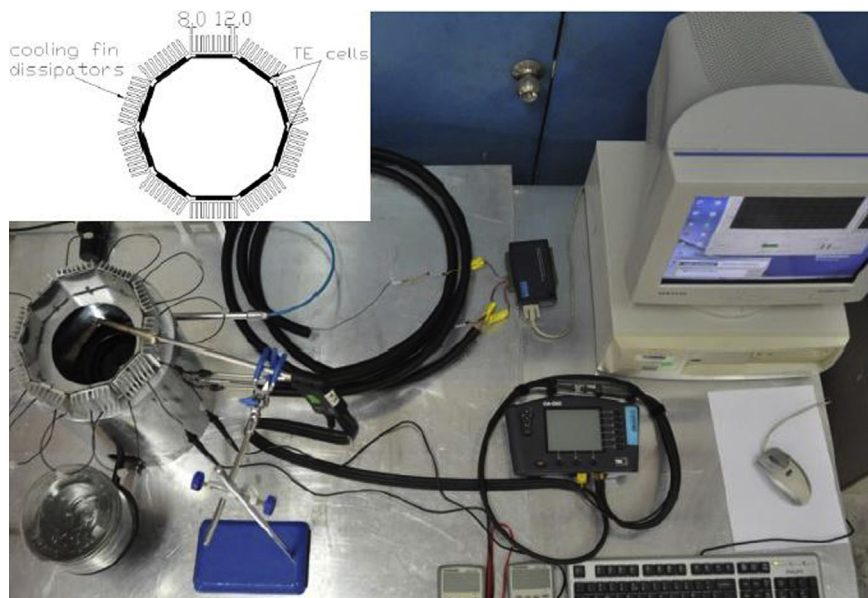


Fig. 2. Experimental set-up and TE cells with cooling fin dissipators.

An electronic mass balance (BX32KH Shimadzu, Japan), with a 32 kg range and 0.001 kg resolution, supported the fuel container. Fuel consumption was calculated by recording the time and weight reduction of the whole system over a certain period. The tangential air flow rate into the cylindrical combustion chamber was controlled by a mass flow meter (CMS Massflow, Yamatake Corporation, Japan) calibrated using a bubble flow meter in the range of 0–500 L/min. The supplied air passed through a pressure regulator, and a water trap was used to remove the moisture.

Measurement of axial temperature distribution within the flame holder was recorded using an Advantech 4718 data acquisition system (Advantech Company Limited). Four thermocouples were included in the burner: three were located in the flame holder chamber and one at the entrance of the tangential air flow into the cylindrical combustion chamber. The thermocouples in the flame holder combustion chamber recorded the flame, exit gas, and porous alumina surface temperatures. These thermocouples were nickel–chromium (type K) thermocouples (Omega Engineering Inc., USA). The thermocouples in the flame holder combustion chamber were precisely positioned at three different locations in

the axial direction from the surface of the porous alumina: 0 mm (T_1), 50 mm (T_2), and 100 mm (T_3). These details are illustrated in Fig. 4.

Products of combustion gases were measured and analyzed to assess the combustion characteristics of the burner. Oxides of nitrogen (NO_x) and carbon monoxide (CO) were continuously sampled using a CA-6203 CA-CALC combustion analyzer (TSI Incorporated, USA) equipped with a standard water trap filter to remove the moisture from the combustion products. The accuracy of the analyzer for NO_x detection was ± 5 ppm (0–100 ppm) and ± 10 ppm (100–4000 ppm), with a resolution of 1 ppm, whereas that for the CO readings was ± 5 ppm (0–100 ppm) and ± 10 ppm (100–5000 ppm), with a resolution of 1 ppm. The reaction time was approximately 30 s, which was automatically calibrated through its zero calibration function during daily start-up procedure.

Ten Bismuth-Telluride TE cells (Everredtronics Ltd., China) were attached to a 1 mm-thick stainless steel plate fabricated into a ten-sided polygon. These cells form the TE modules. The hot side of the plate was continually exposed to the hot exhaust gases of the combustion products during the experiment. The finned dissipators made of aluminum plates were thermally glued to the cold side of the TE modules to create temperature gradient for TE power generation. The temperatures of the hot and cold sides were measured by K-type thermocouples placed at appropriate locations. Thermal grease was used in creating a conductive phase environment to enhance the heat transfer by conduction mode between the hot side combustion chamber and the cold fins and reduce the thermal contact resistance [24]. Ten finned dissipators, composed of rectangular stainless steel base plate, were attached to the TE module. The dimensions of each individual fin dissipator are shown in Fig. 2. The TE cells were connected in series, in which the output terminal from each individual TE cell was connected to the input terminal of the adjacent cell. The output terminal of the last cell was loaded with a variable electrical resistor connected to a GDM 394 multimeter (GW Instek, Taiwan). The electric power output generated by the cells was calculated based on the voltage and current produced, with the loaded resistance recorded by the multimeter. The physical sizes and relevant characteristics of the TE cell are listed in Table 2.

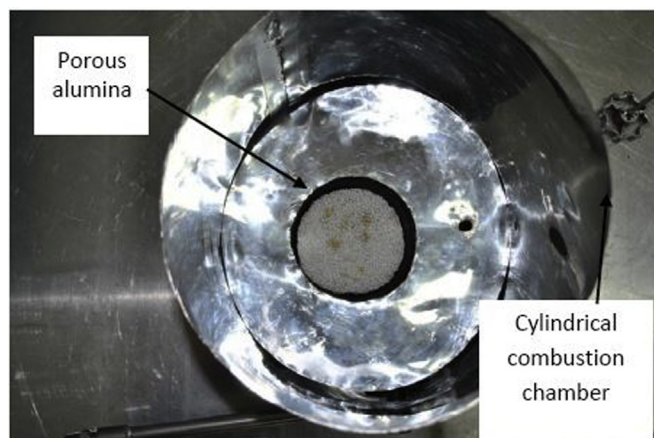


Fig. 3. Top view of the cylindrical combustion chamber with porous alumina.

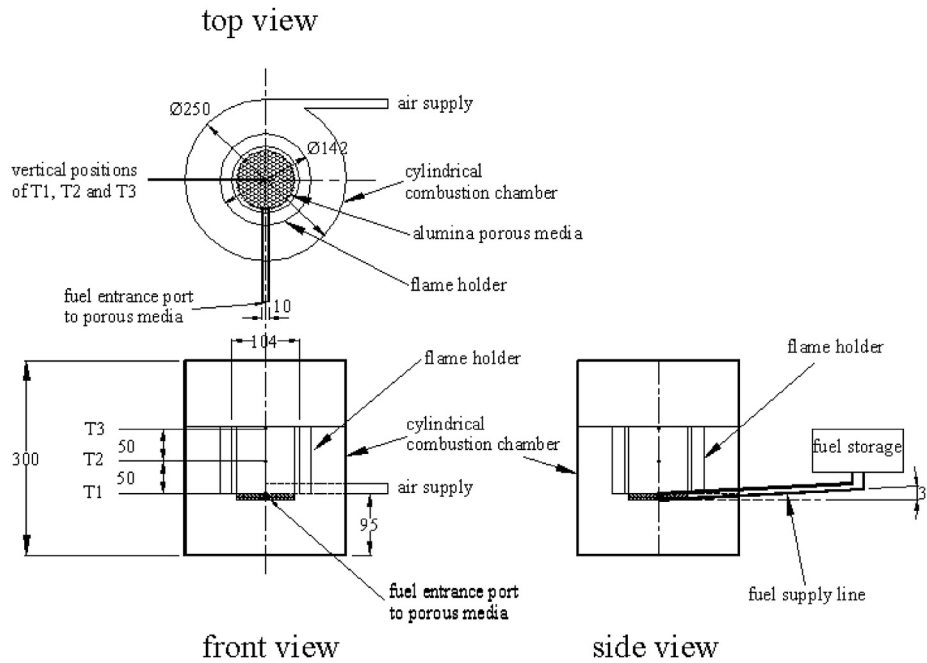


Fig. 4. Detail layout of the combustion chamber (all dimensions are in mm).

2.3. Methods

The underlying concept of the whole proposition in this study was to investigate the combustion characteristics of the porous alumina burner and the corresponding electrical power output using the TE module at several values of fuel–air equivalence ratio. In principal, the entire study involves detailed mapping between the combustion characteristics of the liquid fuel-fired burner and the electrical power output of the TE module. Operating the porous alumina burner was first initiated by adjusting the fuel control valve to the minimum opening to allow fuel to flow into the porous alumina housing. Capillary action ensured that the fuel was adequately soaked by the porous alumina before ignition. The soaking duration needed before ignition did not significantly vary for all types of fuels tested, which ranged from approximately 2 to 4 min. The required soaking duration did not exhibit any specific pattern for all blends of fuels tested, but sufficient wetting of the porous alumina reduced the amount of time needed to achieve steady state condition to sustain combustion. A propane pilot flame was used to ignite the fuel vapors, which was later removed after stable flame was fully achieved and anchored in the porous alumina. The swirling air supply into the cylindrical combustion chamber was precisely monitored using an airflow meter (CMS Massflow, Yamatake Corporation, Japan). This amount of air supplied to the chamber was predetermined based on calculated theoretical values to cover from the richest to the leanest fuel–air equivalence ratios. However, the actual fuel–air equivalence ratios for all tested fuels were precisely recalculated later based on the

ratio of the stoichiometric air–fuel ratio and the exact air and fuel flow rates. Although the predetermined and actual fuel–air equivalence ratios were not exactly similar, slight variations were observed. The actual fuel–air equivalence ratios sufficiently covered the intended range from the leanest to the richest mixture ratios.

The surface temperature of the porous alumina was continuously recorded and the burner was allowed to run until steady state temperature was reached. The temporal temperature distributions of the steady state condition for all blends of tested fuels are shown in Fig. 5. The time required to achieve a steady state temperature increased with the increase in VCO content in the fuel blends. After reaching the steady state condition, all axial temperatures in the flame holder (T_1 , T_2 , and T_3) were simultaneously recorded and stored by a data logger (8-channel thermocouple input, Advantech USB4718, Advantech Company Limited) for further processing. The fuel consumption was also recorded and the fuel flow rate was calculated based on the weight reduction of the fuel container and the time elapsed during the burner operation.

Surface temperature profiles of the porous alumina during combustion were captured using the Fluke Ti27 thermal imager (Fluke Corporation, USA). These instantaneous images complemented the point surface temperature measurement, T_1 , measured with a K-type thermocouple. Gaseous emissions of NO_x and CO were continuously measured with a CA-6203 CA-CALC combustion analyzer. The sampling probe was placed above the TE module where the flame exits the cylindrical combustion chamber (Fig. 1). Data were sampled and stored in the combustion analyzer memory. The voltage and current output of the TE module were recorded using a multimeter (GDM 394 GW Instek, Taiwan). After recording and storing the temperatures, emissions, and electrical output data, the air supply to the primary cylindrical combustion chamber was slowly increased to the desired predetermined value to change the fuel–air equivalence ratio. The whole procedure was repeated at a new fuel–air equivalence ratio. When the entire experiment for a specific blend of fuel was completed, the porous alumina was dried for up to three days prior to testing with another fuel blend.

Table 2
Physical sizes and characteristics for each thermoelectric cell.

Thermoelectric cell	
Model number	TEG1-241-1.0-1.2
Length × width × height (mm ³)	40 × 40 × 3.6
Open circuit voltage, V_{oc} (V)	12.1
Load power, W	3.6
Maximum temperature difference, ΔT (°C)	200

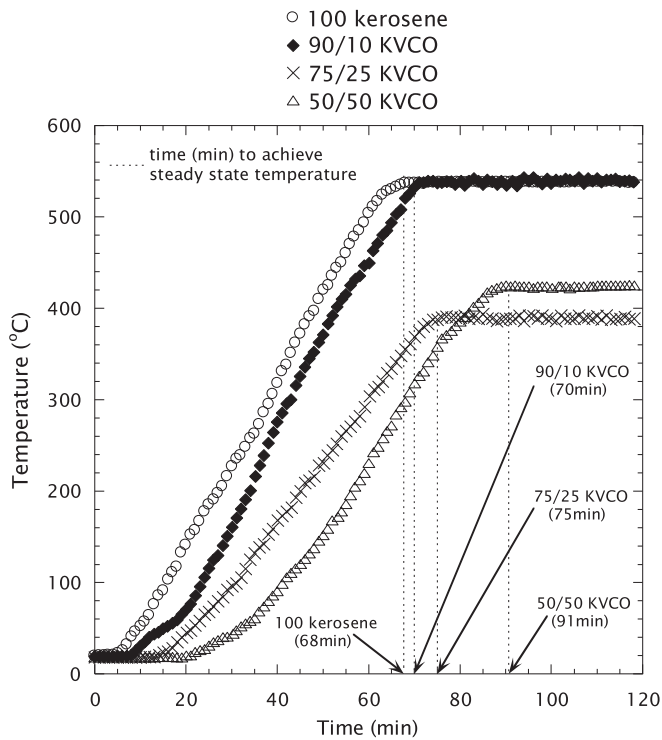


Fig. 5. Temporal distributions of steady state temperatures for all blends of fuels.

2.4. Experimental uncertainty

The measured data for temperatures T_1 , T_2 and T_3 , mass flow rate of air, \dot{m}_a mass flow rate of fuel, \dot{m}_f voltage, current and exhaust emissions of CO and NOx are listed in Table 3. Experiments were repeated three times and the recorded values are shown in Table 3.

For all measured data, the mean value (\bar{X}) and standard deviation (S_X) can be expressed as [24,50]:

$$\bar{X} = \frac{1}{n} \sum_{i=1}^n X_i \quad (1)$$

$$S_X = \left[\frac{1}{n-1} \sum_{i=1}^n (X_i - \bar{X})^2 \right]^{1/2} \quad (2)$$

Uncertainty is defined as [24]:

$$\text{Uncertainty} = \frac{\text{Standard deviation}}{\text{Mean value}} \times 100\% \quad (3)$$

The calculated mean values, standard deviation and uncertainty are shown in Table 4. Sample data at specific values of ϕ are selected for all blends of fuels.

The uncertainty for all measured data is reliable and acceptable since it ranges from 0.0% to 3.4%.

3. Thermodynamics of combustion

The ultimate analysis was carried out to determine the stoichiometric combustion equation for 100 kerosene and other blends of kerosene with VCO (90/10 KVCO, 75/25 KVCO, and 50/50 KVCO) to find the stoichiometric air–fuel ratio from the combustion equation. An elemental analyzer (EA Perkin Elmer CRIESII 2400, Perkin Elmer, USA) was used for this analysis and the results are shown in Table 5. The stoichiometric combustion equation can be written as follows:



where “ a ” can be expressed in terms of x , y , and z to obtain the following equation:

$$a = x + \frac{y}{2} - z. \quad (5)$$

The stoichiometric air–fuel ratio A/F_s on a mass basis can be written as follows:

$$\frac{A}{F_s} = \frac{a[32 + 3.76(28)]}{12x + 2y + 32z} = 34.32 \left(\frac{2x + y - 2z}{6x + y + 16z} \right) \quad (6)$$

where the molecular weight M for O_2 and N_2 is 32 and 28, respectively.

4. Results and discussion

4.1. Porous media characterization

The porous alumina Al_2O_3 was examined by scanning electron microscopy (S-3400N SEM, Hitachi, Japan) to study the surface morphology and structural integrity. However, given the space limitation and scope of this study, only the SEM figures with 75/25 KVCO are presented. The 75/25 KVCO was arbitrarily chosen because this blend was used in the third cycle of the experiment (after 100 kerosene and 90/10 KVCO); hence, any structural deformation or micro structural changes would have gradually shown physical signs of reaction to combustion. Fig. 6 shows the magnifications both (A) before and (B) after combustion. The micrographs of the structure illustrate the inhomogeneity of the pore distribution and sizes throughout the porous alumina before and after

Table 3
Experimental data.

Variable	Fuel											
	100 kerosene (At $\phi = 1.04$)			90/10 KVCO (At $\phi = 0.97$)			75/25 KVCO (At $\phi = 1.04$)			50/50 KVCO (At $\phi = 1.06$)		
	1st	2nd	3rd	1st	2nd	3rd	1st	2nd	3rd	1st	2nd	3rd
T_1 (°C)	578.7	582.3	581.8	541.2	540.4	547	545.9	553.5	550.1	500.4	504.1	505.4
T_2 (°C)	391.5	400.4	392.7	431.9	428.9	435.4	404.41	403.56	399.6	387	385.4	389
T_3 (°C)	323.7	324.9	331.9	386.26	388.55	387.55	328.23	328.40	331.40	286.346	288.215	287.31
\dot{m}_a ($\times 10^{-4}$)	3.0309	3.04953	3.03804	2.94712	2.94824	2.94793	2.8760	2.8750	2.8800	2.39119	2.39132	2.39134
\dot{m}_f ($\times 10^{-5}$)	1.9072	1.9130	1.9107	1.98148	1.98134	1.98152	1.91636	1.91656	1.91647	1.80288	1.80288	1.80288
V	34	34	34	49	51	50	44.80	44.82	44.28	44.8	44.9	45
I	0.53223	0.5251	0.503	0.5641	0.56248	0.5637	0.3199	0.3145	0.3296	0.44	0.47	0.45
CO	855	847	851	900	894	897	636	637	629	488	495	490
NOx	1	1	1	0	0	0	3	3	2	3	3	3

Table 4

Uncertainty of the experimental data.

Fuel	Variable								
	T_1 (°C)	T_2 (°C)	T_3 (°C)	$\dot{m}_a (\times 10^{-4})$ kg/s	$\dot{m}_f (\times 10^{-5})$ kg/s	V Volt	I Amp	CO ppm	NOx ppm
100 kerosene									
Mean value	580.9	394.8	326.8	3.03949	1.9103	33.73	0.5201	851	1
Standard deviation	1.9	4.8	4.4	0.00940	0.0029	0.46	0.0152	4	0
Uncertainty	0.3%	1.2%	1.4%	0.3%	0.2%	1.4%	2.9%	1.0%	0.0%
90/10 KVCO									
Mean value	542.8	432.0	387.4	2.94776	1.98145	50.00	0.5634	897	0
Standard deviation	3.6	3.3	1.1	0.00578	0.00945	1.00	0.0008	3	0
Uncertainty	0.7%	0.8%	0.3%	0.0%	0.0%	2.0%	0.1%	0.3%	0.0%
75/25 KVCO									
Mean value	549.8	402.5	329.3	2.877	1.91646	44.63	0.3213	634	3
Standard deviation	3.8	2.6	1.8	0.00265	0.00100	0.31	0.0077	4	0
Uncertainty	0.7%	0.6%	0.5%	0.1%	0.0%	0.7%	2.4%	0.7%	0.0%
50/50 KVCO									
Mean value	503.3	387.1	287.2	2.39128	1.80288	44.90	0.45	491	3
Standard deviation	2.6	1.8	0.9	0.00814	0.00251	0.10	0.015	4	0
Uncertainty	0.5%	0.5%	0.3%	0.0%	1.4%	0.2%	3.4%	0.7%	0.0%

Table 5

Ultimate analysis and calculated stoichiometric air–fuel ratio.

Fuel	Ultimate analysis (weight %)					Stoichiometric air–fuel ratio
	C	H	O	N	S	
100 kerosene	71.31	24.63	3.18	0.53	0.35	16.6
90/10 KVCO	74.65	17.52	6.24	0.60	0.99	14.5
75/25 KVCO	79.88	18.43	0.45	0.22	1.02	15.6
50/50 KVCO	70.72	18.22	9.73	0.25	1.08	14.0

testing. The matrix intricate between the pore and the solid structure can be clearly observed in the figure, which is essential for enhancing heat transfer during combustion. Although the porous alumina was subjected to a series of combustion reaction, the extremity of the combustion does not substantially affect the structural integrity of the porous alumina. External impurities were not detected in the microscopic figures, and the overall matrix was free from any unknown deposits.

4.2. Ultimate analysis and stoichiometric air–fuel ratio

The ultimate analysis and stoichiometric air–fuel ratio is tabulated in Table 5.

4.3. Temperature profiles

The centerline temperature distributions along the cylindrical combustion chamber axis for all blends of fuels are presented in Fig. 7A–D. These temperature profiles were measured at the porous

alumina surface, T_1 , at an upper vertical distance of 50 mm from the porous alumina surface, T_2 , and near the flame exit location of the flame holder, T_3 (100 mm from the porous alumina surface). The instantaneous thermal images are also shown at several data points of fuel–air equivalence ratio to complement the point temperature measurements T_1 at the porous alumina surface. Appropriate analysis of these images was carried out to obtain qualitative understanding and provide explanation of the combustion process for porous alumina. All measured temperatures were plotted against a range of fuel–air equivalence ratio ϕ representing a lean combustion ($\phi < 1$) and a rich combustion ($\phi > 1$) regime. To vary the fuel–air equivalence ratio, both air and fuel flow rates were gradually changed during the experiment to cover extensive data points of ϕ in the lean combustion regime with a step difference of about 0.10 between each data points. Meanwhile, the rich combustion regime was extended to a maximum ϕ value of about 2.50, with only three or four data points. For useful comparison, the desired values of ϕ for all tested fuels were initially intended to be similar. However, given that the stoichiometric air–fuel ratio for each tested fuel differs marginally, changing both air and fuel flow rates during the experiment consequently leads to slight variations of ϕ for all fuels blends.

Fig. 7 reveals the essential thermal structure features in terms of temperature profiles for porous alumina and within the combustion chamber. A general trend for all blends of fuels in the range of ϕ evaluated was observed in Fig. 7, which indicates greater T_1 temperatures compared with T_2 and T_3 . The temperature distributions of T_1 were in the range of 440 °C–730 °C. For 100 kerosene, T_1 was in the range of 520 °C–720 °C, which was significantly higher than

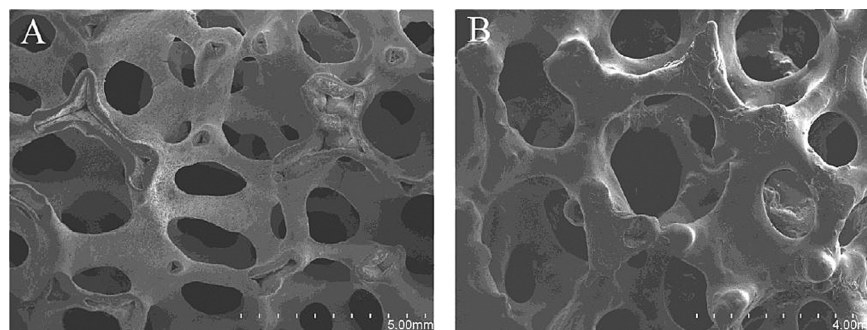


Fig. 6. SEM figures of porous alumina, Al_2O_3 . (A) before combustion and (B) after combustion.

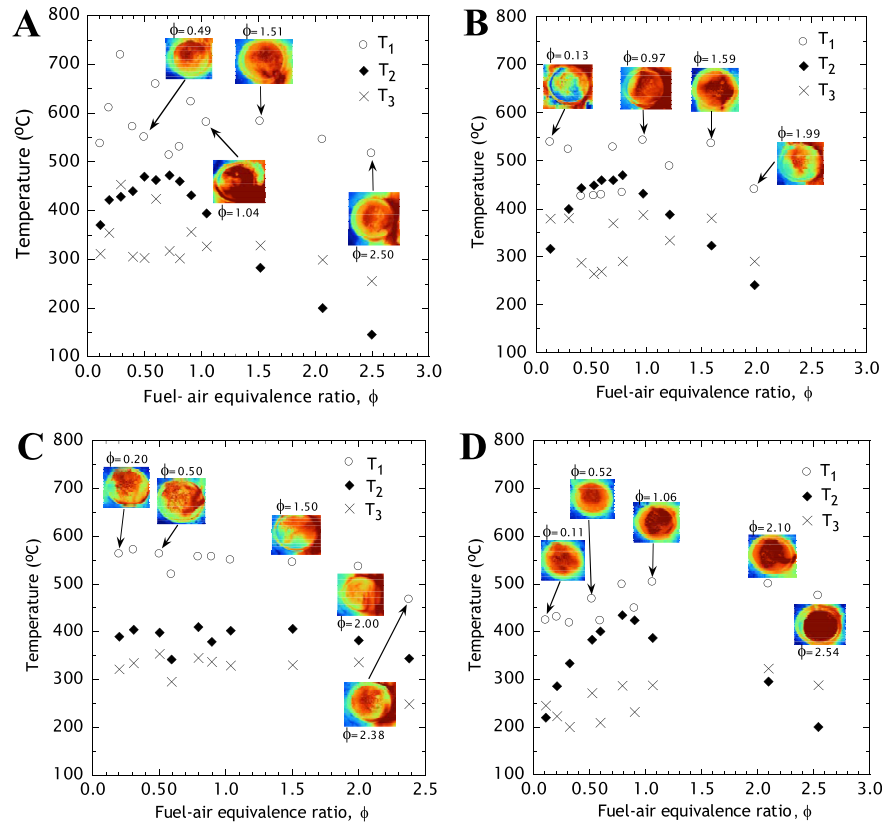


Fig. 7. Fuel-air equivalence ratio against temperatures T_1 , T_2 and T_3 . T_1 is the central surface temperature of the porous media; T_2 is the central flame temperature inside the concentric double-cylinder combustion chamber at an axial distance of 50 mm from the surface of porous alumina surface; T_3 is located at central vertical distance of 100 mm from the surface of porous alumina (A) 100 kerosene (B) 90/10 KVCO (C) 75/25 KVCO and (D) 50/50 KVCO.

the boiling temperature of kerosene (250 °C) [41]. Despite the non-uniformity of the temperature profiles spreading in the range of ϕ evaluated, complete combustion took place at the porous alumina surface, as closely observed in Fig. 7A. Flame images at various data points of ϕ show that thermal radiation from porous alumina provides energy feedback at most locations, indicating sufficient flame stabilization at the porous alumina surface. Moreover, the combustion in the lean and rich regime yielded stable flames, as indicated by the orange flames of the porous alumina. For 90/10 KVCO, 75/25 KVCO, and 50/50 KVCO (Fig. 7B–D) T_1 temperature displayed better uniformity and only mildly fluctuates compared with 100 kerosene in the range of ϕ values evaluated. The maximum temperatures recorded for these fuel blends were considerably lower (542 °C for 90/10 KVCO, 571 °C for 75/25 KVCO, and 503 °C for 50/50 KVCO), but similarly peaked at lean region of combustion. Thermal images for both 90/10 KVCO and 75/25 KVCO showed greater enhancement of flame stability, with orange flame captured in the lean combustion region. However, the formation of soot in the rich combustion zone for the 50/50 KVCO was fairly noticeable, which can be attributed to the emission of unburned hydrocarbon. T_2 temperature was measured to assess the developed flame temperature; T_3 temperature served as a ‘guide’ temperature prior to the entrance of the TE module close to the burner exit. Given that the power output generated by the TE modules was heavily dependent on the temperature gradient across the modules, T_3 temperature was arbitrarily used in designing and selecting the cooling fin dissipators for the TE module in this study. For the 90/10 KVCO and 75/25 KVCO, T_2 temperature was marginally higher than T_3 in most places, indicating a consistent reduction in temperature because of heat loss in the flame holder. For the 50/50

KVCO fuel blend, T_2 temperature gradually increased in tandem with ϕ and exhibited maxima at close to stoichiometric ratio. However, T_2 temperature drastically deteriorated as the mixture was enriched beyond stoichiometric. The T_2 temperature curve for the 50/50 KVCO (Fig. 7D) showed similar resemblance to 100 kerosene and 90/10 KVCO fuel blends, although steeper rise of T_2 was observed at the lean region when $\phi < 1$. Increase or decrease in ϕ values virtually affected T_3 temperatures for 100 kerosene and 90/10 KVCO; however, the distribution remained unchanged for 75/25 KVCO and 50/50 KVCO.

4.4. Power output against temperature difference

The dependency of temperature gradient between the hot source and cold junction is essential for TE power generation, indicating that the influence of hot source temperature need to be explained because low-temperature heat input to the TE cells is usually associated with reduced performance of the TE system [24]. For the combustion-based TE system proposed in this work, the temperature difference between the porous alumina surface T_1 and the exit temperature of the burner T_3 provided reasonable indicator of the input temperature to the TE module in the burner system. Fig. 8 shows the influence of temperature difference, ΔT ($T_1 - T_3$) on the power output of the TE modules. The power output range was demarcated by the minimum and maximum values of 4.9 W and 21.9 W, respectively. The effects of ΔT on power output at all data points, was rather inconclusive, as shown by the scatters lying either at high ΔT (more than 200 °C) or low ΔT (less than 200 °C). To some degree, this trend is valuable because it indicates the non-dependency of ΔT towards power generation. In addition, the

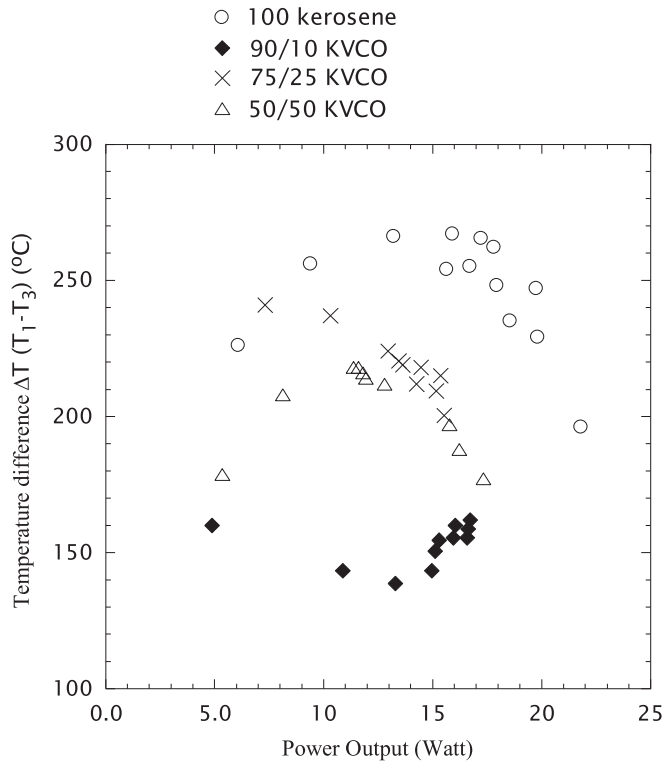


Fig. 8. The distributions of temperature difference, $\Delta T (T_1 - T_3)$ against power output for all blends of fuel mixtures tested in this study.

wide range of power output against ΔT allows greater degree of freedom in controlling the ϕ over the intended power output of the TE system. Moreover, despite the inherent differences in the thermophysical properties of the tested fuels, the generated power output is only marginally sensitive towards the characteristics of the fuel blend.

4.5. Fuel–air equivalence ratio against electrical efficiency

The electrical efficiency at various ϕ values for all blends of tested fuels is plotted in Fig. 9. The ϕ values are similar to those discussed in Section 4.3. Electrical efficiency was calculated based on [16] and expressed as follows:

$$\eta_{\text{elec}} = \frac{P_{\text{TE}}}{\dot{m}_f \times Q_{\text{net}}} \quad (7)$$

where P_{TE} is the electric power output from TE module, \dot{m}_f is the fuel flow rate, and Q_{net} is the lower heating value of the fuel blends (Table 1). The flow rate and lower heating value produces the chemical power of the fuel. The hot exhaust gas provides continuous heat source by heating the inner wall of the aluminum plate. TE cells were electrically connected in series, but thermally connected in parallel to form TE module. Fig. 9 shows the electrical efficiency against ϕ based on the calculated values of the chemical power and measured electric power output at each test conditions. The effect of ϕ on electrical efficiency is distinctly characterized by the following patterns: (i) a maximum electrical efficiency at close to stoichiometric for 100 kerosene and 90/10 KVCO and (ii) an approximate linear reduction of electrical efficiency for 75/25 KVCO and 50/50 KVCO as ϕ is gradually enriched.

For 100 kerosene and 90/10 KVCO, the relationship between the electrical efficiency curves and ϕ are principally characterized

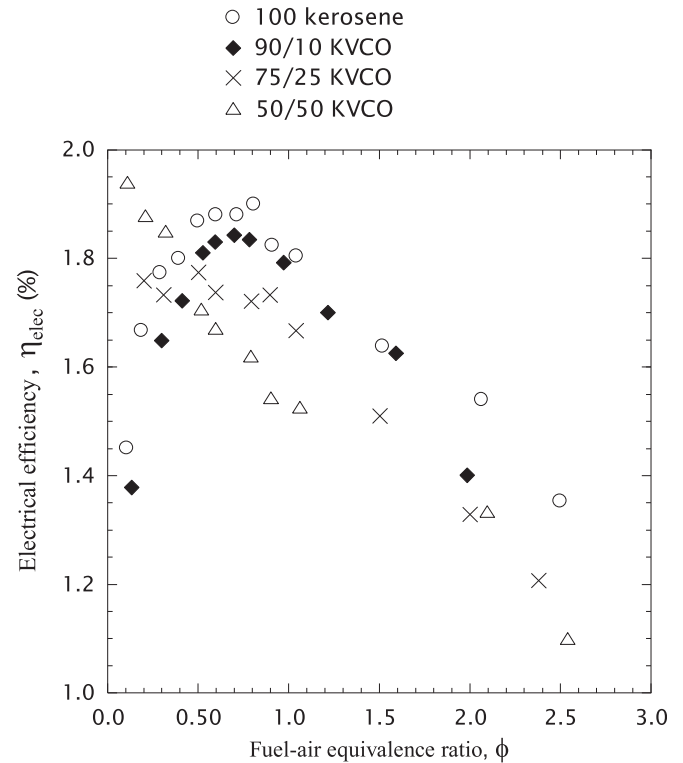


Fig. 9. Electrical efficiency distribution against fuel-air equivalence ratio.

by maximum efficiency at lean, but close to stoichiometric mixture (maximum $\eta_{\text{elec}} = 1.9\%$ at $\phi = 0.80$ for 100 kerosene and maximum $\eta_{\text{elec}} = 1.84\%$ at $\phi = 0.70$ for 90/10 KVCO). The influence of ϕ towards electrical efficiency at both lean and rich regions showed noticeable deterioration when ϕ was reduced to less than the aforementioned maximum electrical efficiency, or when ϕ was further enriched beyond the maximum values. Both tested fuels exhibited relatively low electrical power output during lean operating conditions, which may explain the considerable drop in the TE module efficiency. Meanwhile, the diminishing values of electrical efficiency at higher ϕ in rich mixture conditions can be attributed to the minimal change of fuel mass flow rate, and thus the input chemical energy to the system. Power output is also adversely affected, thereby aggravating the electrical efficiency. Experiments with 75/25 KVCO and 50/50 KVCO indicated an approximately linear reduction in electrical efficiency as ϕ swept from lean to rich mixtures. The highest and lowest electrical efficiency for 75/25 KVCO was 1.77% at $\phi = 0.50$ and 1.20% at $\phi = 2.38$, respectively. Although the highest electrical efficiency was not at the leanest condition, the calculated electrical efficiency still occurred at a leaner side of the mixture. For the 50/50 KVCO, the electrical efficiency deteriorated appreciably as ϕ was increased from lean to rich mixtures. The highest electrical efficiency attained was 1.94% at $\phi = 0.10$, and linear reduction was observed as ϕ was enriched with a minimum value of 1.10% at $\phi = 2.54$. Regardless of ϕ , the highest and lowest electrical efficiency for 50/50 KVCO were also the highest and lowest values among all the tested fuels.

4.6. Fuel–air equivalence ratio against voltage, current, and power output

The load voltage, current, and power plot against ϕ is shown in Fig. 10 for 100 kerosene and its blends with varying fractions of

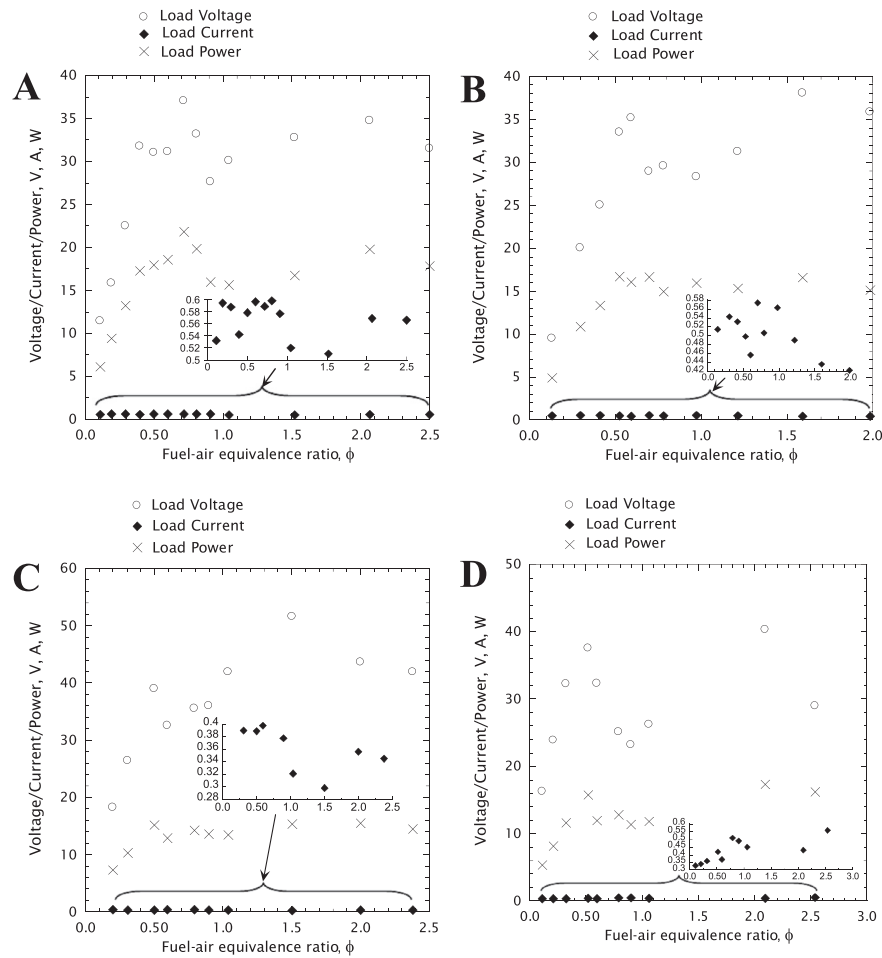


Fig. 10. Load voltage, current and power output against fuel–air equivalence ratio (A) 100 kerosene (B) 90/10 KVCO (C) 75/25 KVCO and (D) 50/50 KVCO.

VCO. Voltage and current output were measured using a multi-meter, and the generated power was calculated as follows [43]:

$$P = IV = \frac{V^2}{R} \quad (8)$$

In all cases, the generated current was small, ranging from a minimum value of 0.33A to a maximum value of 0.60A. Although sporadic distribution of electrical current generated was recorded for the range of ϕ evaluated in this study, close examination of the data revealed an increasing trend of maximum and minimum values of load current from 100 kerosene to 50/50 KVCO. Given that the current output was negligibly small, as shown in Fig. 10, the output power curve was sensitive to the output voltage response. The observed pattern of power generated was generally characterized by an appreciable increase as ϕ values were slowly increased in the lean region, but stabilized when ϕ exceeded beyond stoichiometric values. The favorable power distribution inferred that the operation of the TE burner system developed in this study can possibly be greatly optimized at the lean region, which would subsequently lead to an overall improvement in fuel consumption. However, care must be practiced in drawing conclusions from the power output generated from this system. The performance of the TE modules connected in series is highly non-uniform and can be substantially affected by the Peltier effect [24]. Furthermore, the geometry of the heat sink incorporated in the TE system must also be carefully considered, which has been

expounded by Wang et al. [44] and found general acceptance, but not covered in detail in the present study.

4.7. Fuel–air equivalence ratio against CO and NOx emission

Fig. 11 shows the experimentally measured CO and NOx concentration levels at various fuel–air equivalence ratios for all blends of the tested fuels. As shown in Fig. 11A, CO exhaust emission sharply increased for 100 kerosene and 90/10 KVCO as ϕ approached stoichiometric ratio. However, as ϕ was further enriched in the rich region, only modest increment was recorded. The CO emitted by 100 kerosene fuel was fractionally higher than 90/10 KVCO when $\phi < 1$, but the net formation of this emission became marginally lower in the rich region when $\phi > 1$. This behavior is consistent for both 100 kerosene and 90/10 KVCO because majority of corresponding equivalence ratio varied during the test. In addition, the highest level of CO emission recorded for 100 kerosene (926 ppm at $\phi = 2.49$) was slightly lesser than that for 90/10 KVCO (989 ppm at $\phi = 1.99$). The exhausted CO emissions tend to closely follow the soot emitted by the burner, which is attributed to the chemical mechanisms [42]. In the range of ϕ investigated in the present study, the variation of CO emission for 50/50 KVCO appeared to be reduced fairly substantially especially in the lean combustion region. Increasing trend of CO emission was observed, starting with the lowest value of 177 ppm at $\phi = 0.10$ and reaching 491 ppm close to the stoichiometric value of $\phi = 1.07$. These values represent approximately one-half to two-thirds of the

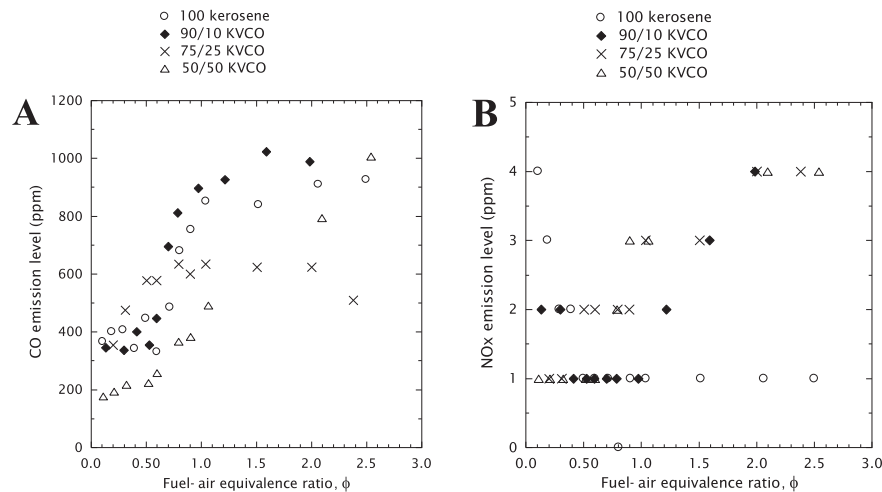


Fig. 11. Measured emission level (ppm) at various fuel-air equivalence ratios: (A) CO and (B) NOx.

corresponding values compared with 100 kerosene and 90/10 KVCO. The desirable effect of combustion temperature on the porous media surface is noticeable, which has a significant role in the amount of CO emission exhausted. The surface temperature T_1 of the porous media (Fig. 7D) is generally lower, but sufficient to produce complete combustion of the burner. Complete combustion was achieved despite the higher viscosity value for 50/50 KVCO compared with other blend of fuels that would theoretically impair mixing efficiency prior to combustion. The CO emission for 75/25 KVCO was strikingly similar when $\phi < 1$, but appeared to be less affected by the value of ϕ when the blend was further enriched. The insensitivity at richer ϕ is linked to the constant value of the surface temperature T_1 of the porous media.

The corresponding NOx emission levels for the range of ϕ varied in this study for all four blends of fuels are presented in Fig. 11B. NOx emission for 100 kerosene steeply decreased with the increase in ϕ values. Thus, local regions with high temperature at the porous alumina surface between 510 °C and 720 °C aggravated the kinetic rate, significantly resulting in high levels of NOx. The formation of NOx decayed at rich region of combustion, which also showed that the NOx level was virtually unaffected by an increase in the value of ϕ . Blends of the tested fuels other than 100 kerosene showed remarkably similar behavior when ϕ exceeded stoichiometric value. The emission level steadily increased from 1 ppm to 4 ppm as ϕ was incrementally enriched. The level, however, seemed unaffected by the increased portion of VCO in the fuel blends. Meanwhile, the relatively high amount of NOx for 90/10 KVCO at leaner conditions was somewhat peculiar, as other blends of VCO with kerosene did not exhibit the same trend. Although the differences were slight, they possibly follow the reduced temperature and the lack of premixing between the fuel and air in the present study.

5. Conclusions

TE power generation using a liquid fuel-fired porous burner operated on kerosene and kerosene/VCO blends was successfully developed and evaluated. Although experiments were carried out for relatively high viscosity of kerosene/VCO mixtures, lean extinction fuel–air equivalence ratio of up to 0.10 (for 50/50 KVCO fuel blend) was achieved in this study. The performance characteristics of the integrated porous burner with TE modules, as well as the corresponding output voltage, current, and power were evaluated. The surface temperature of the porous media T_1 was generally higher than the developed (T_2) and exit flame

temperature (T_3). A maximum surface temperature of 719 °C was recorded for 100 kerosene fuel, and a minimum surface temperature of 418 °C was detected for 50/50 KVCO fuel. Apart from 100 kerosene fuel at the rich region of combustion, the exit flame temperature T_3 was generally lower than the developed flame in the concentric double-cylinder combustion chamber T_2 . The highest and lowest electrical efficiency attained in this study was 1.94% and 1.10%, respectively for the 50/50 KVCO fuel; these values were obtained at the leanest and richest fuel–air equivalence ratio. Load current was exceptionally small and fell between 4.9 W and 19.8 W. The CO emission showed remarkable sensitivity towards increasing values of fuel–air equivalence ratios, with the exception of 90/10 KVCO, which recorded the maximum as the fuel mixture approached the stoichiometric value. Moreover, NOx pollutant level was generally low and fluctuated between 1 ppm and 4 ppm.

Acknowledgments

This research at the Porous Media Combustion Laboratory, School of Mechanical Engineering Universiti Sains Malaysia (USM) was sponsored by Ministry of Higher Education (MOHE) Malaysia under Fundamental Research Grant Scheme (FRGS) (Grant number: 203/PMEKANIK/6071236). The authors gratefully acknowledge the financial support received during this research work.

References

- [1] Demirbas A. Biofuels securing the planet's future energy needs. *Energy Convers Manage* 2009;50(9):2239–49.
- [2] Demirbas A. Progress and recent trends in biodiesel fuels. *Energy Convers Manage* 2009;50:14–34.
- [3] Demirbas A. Combustion of biomass. *Energy Source Part A* 2007;29:549–61.
- [4] Balat M. Production of biodiesel from vegetable oils. *Energy Source Part A* 2007;29:895–913.
- [5] Balat M, Balat H. A critical review of bio-diesel as a vehicular fuel. *Energy Convers Manage* 2008;49:2727–41.
- [6] Nwafor OMI, Rice G. Performance of rapeseed oil blends in a diesel engine. *Appl Energy* 1996;54:345–54.
- [7] Labeckas G, Slavinskas S. Performance of a direct-injection off-road diesel engine on rapeseed oil. *Renew Energy* 2006;31:849–63.
- [8] Rakopoulos CD, Antonopoulos KA, Rakopoulos DC, Kakaras EC, Pariotis EG. Characteristics of the performance and emissions of a HSDI diesel engine running with cottonseed oil or its methyl ester and their blends with diesel fuel. *Int J Veh Des* 2007;45:200–21.
- [9] Huzayyin AS, Bawady AH, Rady MA, Dawood A. Experimental evaluation of diesel engine performance and emission using blends of jojoba oil and diesel fuel. *Energy Convers Manage* 2004;45:2093–112.
- [10] Pramanik K. Properties and use of *Jatropha curcas* oil and diesel fuel blends in compression ignition engine. *Renew Energy* 2003;28:239–48.

- [11] Natarajan R, Karthikeyan NS, Agarwal A, Sathiyarayanan K. Use of vegetable oil as fuel to improve the efficiency of cooking stove. *Renew Energ* 2008;33:2423–7.
- [12] Wagutu AW, Thoruwa TFN, Chhabra SC, Lang'at-Thoruwa CC, Mahunnah RLA. Performance of a domestic cooking wick stove using fatty acid methyl esters (FAME) from oil plants in Kenya. *Biomass Bioenerg* 2010;34:1250–6.
- [13] Kratzeisen M, Muller J. Effect of fatty acid composition of soybean oil on deposit and performance of plant oil pressure stoves. *Renew Energ* 2009;34:2461–6.
- [14] Barnes CD, Garwood DR, Price TJ. The use of biodiesel blends in domestic vaporizing oil burners. *Energy* 2010;35:501–5.
- [15] Bazooyar B, Ghorbani A, Shariati A. Combustion performance and emissions of petrodiesel and biodiesels based on various vegetable oils in a semi industrial boiler. *Fuel* 2011;90:3078–92.
- [16] Qiu K, Hayden ACS. A natural-gas-fired thermoelectric power generation system. *J Electron Mater* 2009;38(7):1315–9.
- [17] Kajikawa T. Approach to the practical use of thermoelectric power generation. *J Electron Mater* 2009;38(7):1083–8.
- [18] Federici JA, Norton DG, Bruggemann T, Voit KW, Wetzel ED, Vlachos DG. Catalytic microcombustors with integrated thermoelectric elements for portable power production. *J Power Sources* 2006;161:1469–78.
- [19] Fursenko RV, Minaev SS, Chusov DV. Development and experimental investigation of small-sized thermo-electric generator with diffusion combustion. *Thermophys Aeromech* 2011;18(1):43–50.
- [20] Nuwayhid RY, Shihadeh A, Ghaddar N. Development and testing of a domestic woodstove thermoelectric generator with natural convection cooling. *Energy Convers Manage* 2005;46:1631–43.
- [21] Sano S, Mizukami H, Kaibe H. Development of high-efficiency thermoelectric power generation system. *Komatsu Techn Rep* 2003;49(152):1–7.
- [22] Rowe DM, Min G. Evaluation of thermoelectric modules for power generation. *J Power Sources* 1998;73:193–8.
- [23] Casano G, Piva S. Experimental investigation of the performance of a thermoelectric generator based on peltier cells. *Exp Therm Fluid Sci* 2011;35:660–9.
- [24] Chen W-H, Liao C-Y, Hung C-I, Huang W-L. Experimental study on thermoelectric modules for power generation at various operating conditions. *Energy* 2012;46:874–81.
- [25] Weinberg FJ, Rowe DM, Min G, Ronney PD. On thermoelectric power conversion from heat recirculating combustion systems. *Proc Combust Inst* 2002;29:941–7.
- [26] Posthill J, Reddy A, Sivola E, Krueger G, Mantini M, Thomas P, et al. Portable power sources using combustion of butane and thermoelectric. In: *Proc 24th Int Conf Thermoelec*; 2005. p. 520–3.
- [27] Yu C, Chau KT. Thermoelectric automotive waste heat energy recovery using maximum power point tracking. *Energy Convers Manage* 2009;50:1506–12.
- [28] Champier D, Bedecarrats JP, Rivaletto M, Strub F. Thermoelectric power generation from biomass cook stoves. *Energy* 2010;35:935–42.
- [29] Gou X, Xiao H, Yang S. Modeling, experimental study and optimization on low-temperature waste heat thermoelectric generator system. *Appl Energ* 2010;87:3131–6.
- [30] Qiu K, Hayden ACS. Development of a thermoelectric self-powered residential heating system. *J Power Sources* 2008;180:884–9.
- [31] Jiang LQ, Zhao DQ, Guo CM, Wang XH. Experimental study of a plat-flame micro combustor burning DME for thermoelectric power generation. *Energy Convers Manage* 2010;52(1):596–602.
- [32] Rahman MM, Shuttleworth R. Thermoelectric power generation for battery charging. In: *Proc energ manage power delivery (EMPD)*; 1995. p. 186–91.
- [33] Yoshida K, Tanaka S, Tomonari S, Satoh D, Esashi M. High-Energy density miniature thermoelectric generator using catalytic combustion. *J Microelectromech Syst* 2006;15(1):195–203.
- [34] Krishnan S, Karri NK, Gogna PK, Chase JR, Fleuriel J-P, Hendricks TJ. Progress towards an optimization methodology for combustion-driven portable thermoelectric power generation systems. *J Electron Mater* 2012;41(6):1622–31.
- [35] Karim AM, Federici JA, Vlachos DG. Portable power production from methanol in an integrated thermoelectric/microreactor system. *J Power Sources* 2008;179:113–20.
- [36] Kyritsis DC, Roychoudhury S, McEnally CS, Pfefferle LD, Gomez A. Mesoscale combustion: a first step towards liquid fueled batteries. *Exp Therm Fluid Sci* 2004;28:763–70.
- [37] Vijaykant S, Agrawal AK. Effect of porous media configuration on combustion of kerosene. In: *44th AIAA Aerospace Sci Meet Exh Nevada*; 2006. p. 11577–85.
- [38] Periasamy C, Gollahalli SR. Experimental investigation of kerosene spray flames in inert porous media near lean extinction. *Energ Fuel* 2011;25:3428–36.
- [39] Bakry A, Al-Salaymeh A, Al-Muhtaseb A, Abu-Jrai A, Trimis D, Durst F. Low-emission premixed porous inert media (PIM) burner system fueled with vegetable (rapeseed) oil using a flow velocity flame stabilization technique. *Energ Fuel* 2010;24:288–94.
- [40] Peck JJ. Development of a liquid-fueled micro combustor. PhD dissertation. Cambridge: Massachusetts Institute of Technology; 2008.
- [41] Jugjai S, Wongpanit N, Laoketkan T, Nokkaew S. The combustion of liquid fuels using a porous medium. *Exp Therm Fluid Sci* 2002;26:15–23.
- [42] Rakopoulos CD, Rakopoulos DC, Hountalas DT, Giakoumis EG, Andritsakis EC. Performance and emissions of bus engine using blends of diesel fuel with biodiesel of sunflower or cottonseed oils derived from Greek feedstock. *Fuel* 2008;87:147–57.
- [43] Rezaia A, Rosendahl LA. Thermal effect of a thermoelectric generator on parallel microchannel heat sink. *Energy* 2012;37:220–7.
- [44] Wang C-C, Hung C-I, Chen W-H. Design of heat sink for improving the performance of the thermoelectric generator using two-stage optimization. *Energy* 2012;39:236–45.
- [45] Jugjai S, Pongsai C. Liquid fuels-fired porous burner. *Combust Sci Technol* 2007;179(9):1823–40.
- [46] Fuse T, Kobayashi N, Hasatani M. Combustion characteristics of ethanol in a porous ceramic burner and ignition improved by enhancement of liquid-fuel intrusion in the pore with ultrasonic irradiation. *Exp Therm Fluid Sci* 2005;29:467–76.
- [47] Fuse T, Araki Y, Kobayashi N, Hasatani M. Combustion characteristics in oil-vaporizing sustained by radiant heat flux enhanced with higher porous ceramics. *Fuel* 2003;82:1411–7.
- [48] Takami H, Suzuki T, Itaya Y, Hasatani M. Performance of flammability of kerosene and NOx emission in the porous burner. *Fuel* 1998;77(3):165–71.
- [49] Zheng XF, Liu CX, Boukhanouf R, Yan YY, Li WZ. Experimental study of a domestic thermoelectric cogeneration system. *Appl Therm Eng* 2014;62:69–79.
- [50] Beckwith TG, Marangoni RD, Lienhard JH. Mechanical measurements. 6th ed. New Jersey: Prentice Hall; 2007.